

## 1 Fabrication and measurement methods

The device was fabricated on a high-purity, near-intrinsic, natural-isotope [100] silicon substrate, with  $n^+$  ohmic source/drain contacts obtained by phosphorus diffusion. A high-quality, 10 nm thick SiO<sub>2</sub> gate oxide was grown by dry oxidation at 800 °C. P ions were implanted through a 90 × 90 nm<sup>2</sup> aperture defined by e-beam lithography in a PMMA mask. The fluence was chosen to obtain the maximum likelihood of having 3 P atoms in a 30 × 30 nm<sup>2</sup> area, subject to Poisson statistics. The implantation energy was 14 keV, resulting in an average depth of ~ 15 nm below the Si/SiO<sub>2</sub> interface. A 5 s, 1000 °C rapid thermal anneal was performed to activate the donors and repair the implantation damage. The aluminium gates to form the spin readout device and transmission line were defined with e-beam lithography using the process described in Ref. [31]. The barrier (LB and RB) and plunger (PL) gates were written in a first layer, followed by Al thermal evaporation and lift-off. A second layer was employed to write the transmission line and top gate (TG). A final forming gas anneal (400 °C, 15 min., 95% N<sub>2</sub> / 5% H<sub>2</sub>) was performed to reduce the interface trap density to the level of ~ 2 × 10<sup>10</sup> cm<sup>-2</sup> eV<sup>-1</sup>, as measured on devices fabricated with the same process.

The sample was mounted on a high-frequency printed circuit board in a copper enclosure, and thermally anchored to the cold finger of a dilution refrigerator with base temperature  $T_{\text{bath}} \approx 40$  mK. The plane of the chip was oriented parallel to the axis of a wide-bore superconducting magnet, to apply magnetic fields of order 1 T along the [110] direction and perpendicular to the short of the transmission line. Semirigid coaxial lines, fitted with copper-powder filters at the base temperature and RC-filters on the circuit board, connected the sample to the room-temperature electronics. The lowest observed electron temperature was  $T_{\text{el}} \approx 300$  mK. All DC voltages to the gates were provided by optoisolated and battery-powered voltage sources, and added through resistive voltage dividers/combiners to the pulses produced by an arbitrary waveform generator.

We applied compensated pulses using a Tektronix AWG520, to ensure that the pulsing only shifted the donor electrochemical potentials but kept the SET island potential constant. The voltage pulse was applied directly to the top gate, while it was inverted and amplified by a factor  $A$  before reaching the plunger gate (see Fig. 1c of Ref. [8]). The gain  $A$  was carefully tuned to ensure that the SET operating point moved along the top of the SET current peaks, as shown by the blue arrow in Fig. 1d of Ref. [8]. The SET current was measured by a room-temperature transimpedance amplifier, followed by a voltage post-amplifier, a 6<sup>th</sup> order low-pass Bessel filter, and a fast digitising oscilloscope.

The ESR excitations were produced by an Agilent E8257D microwave analog signal generator. The microwave signal was guided to the sample by a semi-rigid coaxial cable ~ 2.2 m in length with a loss of ~ 30 dB at 30 GHz. Gating of the ESR pulses was provided by the Tektronix AWG520, which was synchronised with the TG and PL pulses.

## 2 Electron spin resonance experiment

The ESR experiment consists of a microwave excitation sequence (Fig. S1a) interlaced with voltage pulses (Fig. S1b) applied to the nanostructure of Fig. 1a. It involves two phases: (i) the control phase; where first the (spin-dependent) electrochemical potential of the donor electron  $\mu_{\downarrow/\uparrow}$  is lowered well below that of the electrons in the SET island  $\mu_{\text{SET}}$ , and then a microwave pulse at frequency  $\nu_{\text{ESR}}$  is applied, and (ii) the readout/initialisation phase; where a single-shot projective measurement of the electron spin either results in the detection of a  $|\downarrow\rangle$  or  $|\uparrow\rangle$  state, and leaves the electron initialised  $|\downarrow\rangle$ . If  $\nu_{\text{ESR}}$  coincides with one of the two possible ESR resonances, the electron spin can be excited from  $|\downarrow\rangle$  to  $|\uparrow\rangle$ , which increases the probability of

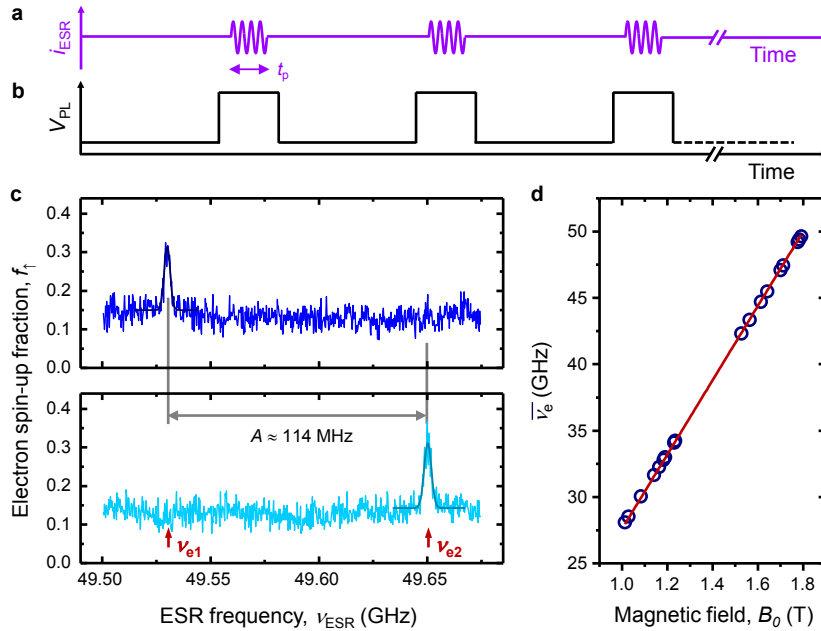


Figure 1: **ESR spectra.** **a-b** Microwave pulse sequence (**a**) and PL gate voltage waveform (**b**) used in the ESR experiment. **c** ESR spectra at  $B_0 = 1.79$  T and with a microwave pulse length of  $t_p = 100\mu\text{s}$ , obtained by counting the occurrence of  $|\uparrow\rangle$  electrons while scanning the ESR frequency. Each data point is obtained from 250 single-shot counts. The nuclear spin is in the state  $|\downarrow\downarrow\rangle$  in the top panel, and  $|\uparrow\uparrow\rangle$  in the bottom panel. **d** Centre ESR frequency,  $\bar{\nu}_e = (\nu_{e1} + \nu_{e2})/2$ , as a function of the external magnetic field  $B_0$ .

detecting a  $|\uparrow\rangle$  state in the readout/initialisation phase.

Fig. S1c shows two measurements of the electron spin-up fraction  $f_{\uparrow}$  as a function of the ESR frequency.  $f_{\uparrow}$  is found for each  $\nu_{\text{ESR}}$  by repeating 250 times the sequence outlined above and counting the number of shots that produce a  $|\uparrow\rangle$  state. The spectra in Fig. S1c were each obtained over 10 minutes and contain a single peak at either  $\nu_{e1}$  or  $\nu_{e2}$ . The ESR pulse sequence is almost identical to that used in the Rabi measurements, but here the microwave pulse length  $t_p$  is  $\gg T_2^*$  ( $= 55$  ns), resulting in an incoherent superposition of the states  $|\downarrow\rangle$  and  $|\uparrow\rangle$ .

From the ESR spectra of Fig. 1c, we extract a hyperfine splitting of  $\sim 114$  MHz, close to the bulk value of 117.52 MHz [32]. We attribute the slight difference in value to a Stark shift brought about by the nearby biased nanostructure device. Fig. S1d shows the ESR centre frequency  $\bar{\nu}_e$  as a function of the external magnetic field  $B_0$ . From the gradient of a linear fit through the data of Fig. S1d, we can extract the electron  $g$ -factor using the relation:

$$\bar{\nu}_e = \frac{\nu_{e1} + \nu_{e2}}{2} = \frac{g\mu_B}{h} B_0, \quad (1)$$

where  $g$  is the Landé  $g$ -factor,  $\mu_B$  is the Bohr magneton and  $h$  is the Planck constant. We find that  $g = 1.98 \pm 0.02$  (accuracy limited by the uncertainty in  $B_0$ ), which is consistent with the bulk measured value of 1.9985 [32].

### 3 Rabi oscillation data analysis

Here we describe in more detail the measurement protocol and the data analysis method employed to obtain the coherent control of the donor electron spin, in the form of Rabi oscillations.

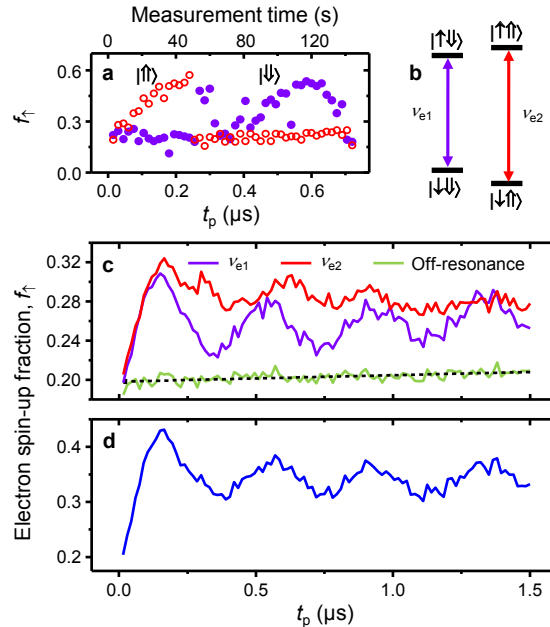


Figure 2: **Rabi oscillation.** **a** Single Rabi sweep at  $P_{\text{ESR}} = 7$  dBm. 250 single-shot electron spin readout measurements are performed at  $\nu_{e1}$  (solid purple circles) and  $\nu_{e2}$  (open red circles) for each  $t_p$ . The top axis displays the time taken to acquire the data. **b** Energy level diagram for the  $^{31}\text{P}$  electron-nuclear spin system, showing the ESR transitions. **c** Averaged Rabi data over 80 sweeps at  $\nu_{e1}$  (purple) and  $\nu_{e2}$  (red). Also shown is the averaged off-resonance spin-up fraction (green) with a linear fit (black dash). **d** Combined  $\nu_{e1}$  and  $\nu_{e2}$  Rabi data, minus the off-resonance contribution.

Following the pulse protocol outlined in Figs. 1e,f, we take 250 single-shot projective measurements of the electron spin, first at  $\nu_{e1}$  and immediately after at  $\nu_{e2}$  ( $\nu_{e1,2}$  are the nuclear-spin dependent ESR frequencies, see Fig. S2b). Fig. S2a shows the electron spin-up fraction  $f_{\uparrow}$  at each frequency as a function of the microwave burst duration  $t_p$ . In this single sweep we observe that at  $t_p \approx 250$  ns the  $^{31}\text{P}$  nuclear spin flips from up to down, and control of the electron spin shifts from  $\nu_{e2}$  to the other hyperfine transition at  $\nu_{e1}$ . Fig. S2c combines 80 of these sweeps, and shows the average  $f_{\uparrow}(t_p)$  for both transition frequencies. Also presented here is the off-resonance electron spin-up fraction (the “false counts”), which is found at each  $t_p$  by taking the minimum  $f_{\uparrow}$  observed at either  $\nu_{e1}$  or  $\nu_{e2}$  for each sweep and averaging over all sweeps.

The off-resonance signal exhibits a linear dependence on the pulse duration, i.e. the “false counts” increase for longer microwave bursts. Since we also observed that the slope is proportional to the microwave power  $P_{\text{ESR}}$ , we attribute this effect to local heating of the electron reservoir caused by the energy delivered by the transmission line. To get the final Rabi plot of Fig. S2d, we sum the averaged  $f_{\uparrow}(t_p)$  plots at  $\nu_{e1}$  and  $\nu_{e2}$  and subtract a fit through the off-resonance background, since at each  $t_p$  the measurement is off-resonance for half of the time.

## 4 Simulation of Rabi oscillations

To simulate the Rabi oscillations of Fig. 2, we assume a decohering noise source with the following properties:

1. It can be modelled by a fluctuating magnetic field  $\Delta B(t)$  along the axis parallel to  $B_0$ . Physically, this can represent the z-component of the hyperfine (often called ‘Overhauser’)

field produced by the bath of  $^{29}\text{Si}$  nuclei on the electron spin;

2. It follows normal (Gaussian) statistics;
3. It changes significantly from one individual measurement (“shot”) to the next, where each measurement lasts  $\sim 1$  ms.

Assumption 3 is non-trivial. We have shown in Fig. 4c that the ESR linewidth for a single sweep is narrower than that observed by ESR in bulk-doped samples, however by averaging several sweeps we recover a bulk-like linewidth (bottom panel of Fig. 4c). The observation of a non-zero width for a single sweep shows that some randomisation of the Overhauser field does occur. We suggest that this is caused by the measurement method we employ, where the electron spin is read out through spin-dependent tunneling. The removal of the electron from the donor causes a large instantaneous change of the total magnetic field at each  $^{29}\text{Si}$  nucleus. Several  $^{29}\text{Si}$  sites have a strongly anisotropic hyperfine coupling. Spins at those sites have a large probability of flipping as a consequence of an electron ionisation / neutralisation event. Conversely, other  $^{29}\text{Si}$  have a very isotropic coupling to the electron spin, and their polarisation is much less influenced by the measurement process. Slow nuclear spin flips at these  $^{29}\text{Si}$  sites are likely to be responsible for the large shift of the central frequency between different sweeps.

In the Rabi experiment, each  $t_p$  point represents an average of 20,000 measurements. Over such a large number of shots, we may safely assume that the Overhauser field (e.g. the configuration of the  $^{29}\text{Si}$  nuclear bath spins) spans the whole permissible range. We therefore generate a weighted distribution of detunings  $d = \gamma_e \Delta B$  from the central values of the ESR frequencies  $\nu_{e1}$  or  $\nu_{e1}$ . The distribution of detunings,  $P(d)$ , is assumed to be a Gaussian function with standard deviation  $\sigma$  and mean  $\mu$ :

$$P(d) = \frac{1}{\sqrt{2\pi}\sigma} \exp\left(-\frac{(d - \mu)^2}{2\sigma^2}\right), \quad (2)$$

where a value of  $\mu \neq 0$  represents an experiment where the frequency of the microwave excitation is shifted from the centre of the resonance line. For each detuning  $d$ , the Rabi oscillation (i.e. the electron spin-up probability as a function of burst time  $t_p$ ) is described by:

$$f_{\text{Rabi}}(t_p, d) = \frac{\Omega_1^2}{\Omega_1^2 + d^2} \sin^2\left(\pi t_p \sqrt{\Omega_1^2 + d^2}\right), \quad (3)$$

The method above yields a model for the decay of the Rabi oscillations as a function of the pulse duration  $t_p$  as caused by a fluctuating Overhauser field. To match the experimental data we must also include non-idealities arising from the finite temperature of the electron reservoir (the SET island) to/from which the electrons tunnel. We define the parameter  $\alpha$  as the probability of a spin-down electron ( $|\downarrow\rangle$ ) tunneling to the SET island during the read phase, and  $\beta$  as the probability of initialising the electron spin-up ( $|\uparrow\rangle$ ) (see Fig. 4b). We define  $P_{\uparrow\text{I}}$  as the probability of having a non-zero fraction of spin-up counts on the off-resonance – “inactive” – hyperfine line (the “false counts” rate), and  $P_{\uparrow\text{A}}$  as the maximum spin-up fraction for the on-resonance – “active” – line.  $P_{\uparrow\text{I}}$  also represents the spin-up fraction at (ideal) Rabi angles  $2\pi, 4\pi, \dots$ , while  $P_{\uparrow\text{A}}$  is the spin-up fraction at (ideal) Rabi angles  $\pi, 3\pi, \dots$ .

The measurement process is non-Markovian in nature. At any given shot, whether or not we load a new electron onto the donor depends on the outcome (spin-up detected or not) of the previous shot. Therefore  $P_{\uparrow\text{I}}$  and  $P_{\uparrow\text{A}}$  must be derived recursively. Calling  $P_{\uparrow\text{I}}(0)$  and  $P_{\uparrow\text{A}}(0)$  the probabilities to detect a spin-up count after a fresh electron load (i.e. loading onto a donor that was certainly ionised), we find the following recursive expressions:

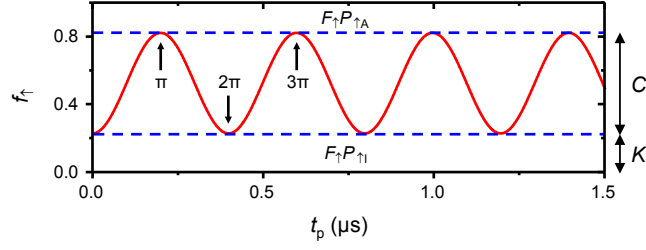


Figure 3: **Rabi simulation model – measurement and thermal effects.** Rabi oscillation with  $F_{\uparrow} = 2.5$  MHz, and  $\sigma = \mu = 0$  MHz, i.e. no fluctuations or resonance offset. This is what a Rabi oscillation would look like in the absence of a fluctuating Overhauser field, but accounting for measurement errors and thermal effects (“false counts” and incorrect initialisation).

$$\begin{aligned}
 P_{\uparrow\downarrow}(0) &= \beta + (1 - \beta)\alpha \\
 P_{\uparrow\downarrow}(i+1) &= P_{\uparrow\downarrow}(i)P_{\uparrow\downarrow}(0) + [1 - P_{\uparrow\downarrow}(i)]\alpha \\
 &= P_{\uparrow\downarrow}(i)\beta(1 - \alpha) + \alpha
 \end{aligned} \tag{4}$$

$$\begin{aligned}
 P_{\uparrow\uparrow}(0) &= (1 - \beta) + \beta\alpha \\
 P_{\uparrow\uparrow}(i+1) &= P_{\uparrow\uparrow}(i)P_{\uparrow\uparrow}(0) + [1 - P_{\uparrow\uparrow}(i)] \\
 &= 1 - P_{\uparrow\uparrow}(i)\beta(1 - \alpha)
 \end{aligned} \tag{5}$$

Finally, we include the imperfections of the measurement with a parameter  $F_{\uparrow}$  that represents the fidelity with which we detect a peak in  $I_{\text{SET}}$  caused by an electron tunneling out of the donor during the readout phase (see Section 5 for more details). Combining this with the thermal initialisation/readout effects, we call  $K = F_{\uparrow}P_{\uparrow\downarrow}$  the observed baseline of the off-resonance counts, and  $C = F_{\uparrow}(P_{\uparrow\uparrow} - P_{\uparrow\downarrow})$  the maximum Rabi oscillation depth, e.g. between (ideal) rotation angles 0 and  $\pi$  (see Fig. S3).

Combining all the effects together yields the following expression for the complete model of the Rabi oscillation experiment:

$$f_{\uparrow}(t_p) = K + C \sum_{d=\mu-5\sigma}^{\mu+5\sigma} P(d)f_{\text{Rabi}}(t_p, d)\Delta d, \tag{6}$$

where  $\Delta d$  is the detuning step-size.

The final step in producing the Rabi simulations is to run a nonlinear least-squares optimisation algorithm to match Eq. (6) to the experimental data, where  $\mu$ ,  $\Omega_1$ ,  $\alpha$  and  $\beta$  are free fitting parameters.  $\sigma$  is fixed at 3.2 MHz, the value extracted from the ESR spectra of Fig. 4c. We chose  $\Delta d$  such that the summation was done over  $\sim 2000$  detunings ( $\Delta d \approx 10$  kHz), a sample large enough that the fitting parameters had converged. We also note that in the above analysis, we have ignored any contribution due to incorrect detection of the  $|\downarrow\rangle$  electron state, since  $1 - F_{\downarrow} \approx 0$ .

## 5 Qubit fidelity analysis

The total system fidelity has been broken down into three categories: (i) measurement, (ii) initialisation and (iii) control. Here we explain and quantify each.

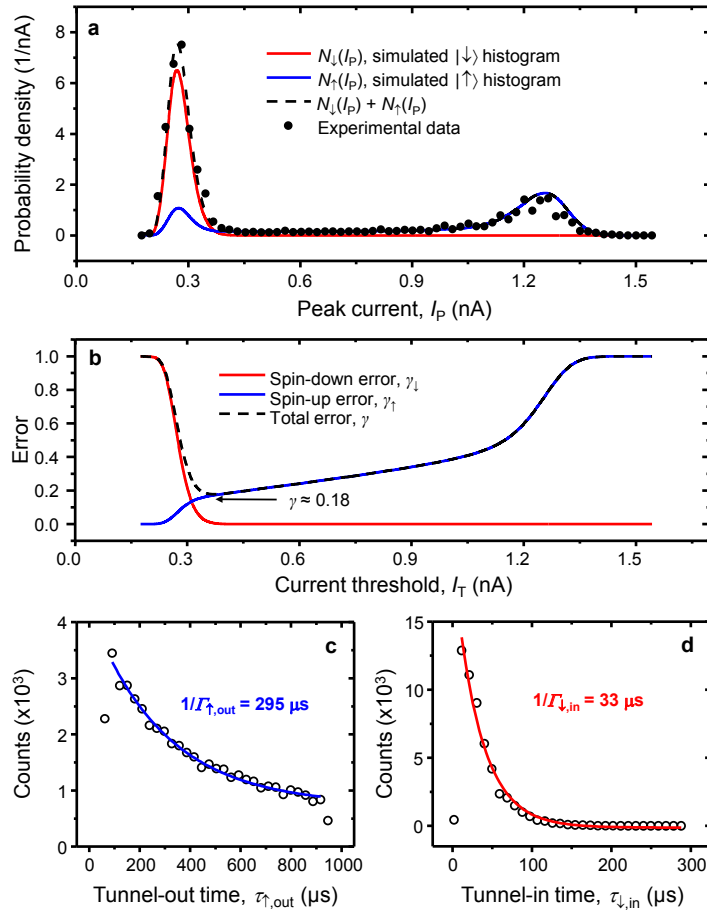


Figure 4: **Measurement fidelity analysis.** **a** Peak current histogram (black circles) for the spin readout signal during the read phase, taken from approximately 125,000 single-shot measurements. Simulations of the peak current histograms for  $|\downarrow\rangle$  and  $|\uparrow\rangle$  electron states are given by the red and blue lines respectively, with the sum by the black dashed line. **b** Electrical readout errors calculated from the simulated histograms of **a**. **c** Electron spin-up tunnel-out time ( $\sim 295 \mu\text{s}$ ) used in the simulations of panel **a**. **d** Spin-down tunnel-in time ( $\sim 33 \mu\text{s}$ ). A delay of  $\sim 10 \mu\text{s}$  between the beginning of the read phase and tunnel events exists, because of the post amplifier and filter chain.

## 5.1 Measurement fidelity

Throughout the readout process there are a number of potential sources of error that can reduce the measurement fidelity. A finite bandwidth can result in an electron spin-up signal (SET current pulse) being missed. Alternatively, electrical noise can cause an incorrect classification of a  $|\downarrow\rangle$  state as  $|\uparrow\rangle$ . We term these electrical readout errors in order to distinguish them from errors arising from thermal effects. Fig. S4a presents the probability densities of peak SET current values for  $|\downarrow\rangle$  and  $|\uparrow\rangle$  electrons during the read phase. The red and blue curves ( $N_\downarrow(I_P)$  and  $N_\uparrow(I_P)$  respectively) are simulations which take a number of parameters as inputs, including the electron spin-up tunnel out time (Fig. S4c) and electron spin-down tunnel in time (Fig. S4d). We refer the reader to Ref. [8] for a detailed explanation of the model used here. The simulation parameters are optimised in order to obtain a good fit to the peak current data (black solid circles in Fig. S4a) extracted from experiment.

With knowledge of the probability densities  $N_\downarrow(I_P)$  and  $N_\uparrow(I_P)$ , one can readily calculate

the electrical readout errors associated with  $|\downarrow\rangle$  and  $|\uparrow\rangle$  electrons by applying (7a) and (7b) respectively. Fig. S4b shows the calculated errors as a function of the discrimination threshold  $I_T$  used when assigning a spin state to a single-shot measurement. We find a minimum total electrical error of  $\gamma = \gamma_\downarrow + \gamma_\uparrow = 0.18 \pm 0.02$  at  $I_T = 370$  pA.

$$\gamma_\downarrow = \int_{I_T}^{\infty} N_\downarrow(I) dI, \quad (7a)$$

$$\gamma_\uparrow = \int_{-\infty}^{I_T} N_\uparrow(I) dI, \quad (7b)$$

With (7a) and (7b), the fidelities used in Section 4 are denoted as  $F_{\downarrow(\uparrow)} = 1 - \gamma_{\downarrow(\uparrow)}$ .

In addition to the electrical readout errors discussed, thermal broadening of the states in the SET island will also contribute to measurement fidelity degradation. The process of a  $|\downarrow\rangle$  electron tunneling to the SET island during the read phase results in the incorrect identification of its spin state. The probability of such an event ( $\alpha$ ) was given as a by-product of the Rabi oscillation simulations in Section 3.

We now define a total measurement error for both  $|\downarrow\rangle$  and  $|\uparrow\rangle$  electrons by combining the electrical and thermal contributions. We denote  $e_{\downarrow(\uparrow)}$  as the total error involved in measuring a  $|\downarrow\rangle$  ( $|\uparrow\rangle$ ) electron, and make the following additional definitions,

$X \Rightarrow$  Incorrectly identify a spin-down electron due to noise exceeding the current threshold

$Y \Rightarrow$  Spin-down electron tunnels to the SET island due to thermal broadening

$Z \Rightarrow$  Incorrectly identify a spin-up electron as a result of the signal not reaching the current threshold

Using the fact that  $X$  and  $Y$  are independent events, but not mutually exclusive, we have,

$$\begin{aligned} e_\downarrow &= P(X \cup Y) \\ &= P(X) + P(Y) - P(X \cap Y) \\ &= P(X) + P(Y) - P(X)P(Y) \\ &= \gamma_\downarrow + \alpha - \gamma_\downarrow\alpha \end{aligned} \quad (8)$$

$$\begin{aligned} e_\uparrow &= P(Z) \\ &= \gamma_\uparrow \end{aligned} \quad (9)$$

This allows us to express the average measurement fidelity as

$$\begin{aligned} F_M &= 1 - \frac{(e_\downarrow + e_\uparrow)}{2} \\ &= 1 - \frac{\gamma + \alpha(1 - \gamma_\downarrow)}{2} \end{aligned} \quad (10)$$

For the  $P_{\text{ESR}} = 10$  dBm Rabi data, we find that  $\alpha = 0.28 \pm 0.01$ . The exact value of  $\alpha$  varies slightly from measurement to measurement, as it depends on the tuning of the electron electrochemical potentials with respect to the SET island. With (10), we find an average measurement fidelity of  $F_M = 77 \pm 2\%$ .

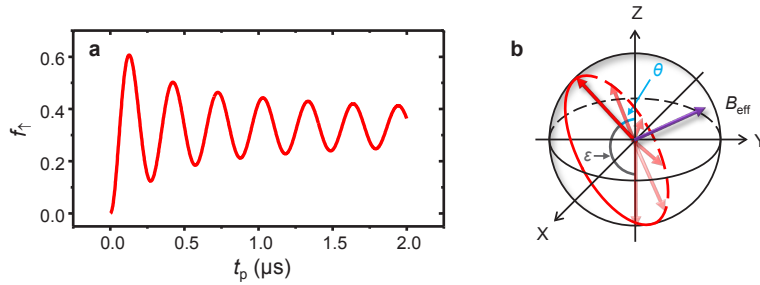


Figure 5: **Pulse error analysis.** **a** Rabi simulation of the  $P_{\text{ESR}} = 10$  dBm data with measurement and resonance offset related errors removed ( $\alpha = \beta = 0$ ,  $F_{\uparrow} = 1$  and  $\mu = 0$ ). **b** Bloch sphere illustrating the effect on control pulses of a  $B_{\text{eff}}$  tilted out of the XY-plane.

## 5.2 Initialisation fidelity

Another by-product of the Rabi simulations was the parameter  $\beta$ . This represents the probability of loading a  $|\uparrow\rangle$  electron (incorrect qubit initialisation). We found  $\beta = 0.01$  with a standard deviation of 0.09 (from the  $P_{\text{ESR}} = 10$  dBm Rabi simulation), giving an initialisation fidelity of  $F_I = 1 - \beta \geq 90\%$ .

The small value of  $\beta$  extracted is consistent with how the measurement is performed. In the experiment we tune the device such that a small amount of random telegraph signal (RTS) exists in the read phase ( $\mu_{\text{SET}}$  is closer to  $\mu_{\downarrow}$  than  $\mu_{\uparrow}$  in Fig. 4b), resulting in a low probability of initialising in the  $|\uparrow\rangle$  state.

## 5.3 Control fidelity

Fluctuations of the local field at the site of the donor (e.g. due to the  $^{29}\text{Si}$  bath spins), add to the generated  $B_1$  field to produce an effective field  $B_{\text{eff}}$  tilted out of the XY-plane in the rotating frame (Fig. 4d). This results in rotation angle errors which we will now examine.

In Section 4 we described how to model the experimental data by including the effect of a fluctuating Overhauser field  $\Delta B(t)$ , plus all the electrical and thermal contributions to the measurement and initialisation errors. Once the model has been matched to the experiment, we may remove all the measurement and initialisation errors to extract the control fidelity, i.e. the Rabi rotation errors occurring solely as a consequence of the random Overhauser field. We use the data set with microwave power  $P_{\text{ESR}} = 10$  dBm, and fix  $\mu = 0$ ,  $\alpha = \beta = 0$  and  $F_{\uparrow} = 1$  to remove the effect of the measurement process and obtain the Rabi oscillations shown in Fig. S5a. The first peak of this plot gives an electron spin-up fraction of  $\approx 0.6$ . This is the average maximum spin-up fraction for an intended  $\pi$  rotation. Representing the state here as  $|\Psi(t_{\pi})\rangle = \eta|\downarrow\rangle + \kappa|\uparrow\rangle$ , we find the average maximum tip angle  $\varepsilon$  (Fig. S5b) to be,

$$|\kappa|^2 = \cos^2\left(\frac{\theta}{2}\right) = 0.6$$

$$\theta = 2 \cos^{-1}\left(\sqrt{0.6}\right) = 78^\circ$$

$$\varepsilon = 180^\circ - \theta = 102^\circ$$

Thus, for an attempted  $180^\circ$  rotation we achieve  $102 \pm 3^\circ$  on average. This gives an average control fidelity of  $F_C = \frac{\varepsilon}{180^\circ} = 57 \pm 2\%$ .



## Supplementary references

31. Angus, S. J., Ferguson, A. J., Dzurak, A. S. & Clark, R. G. Gate-defined quantum dots in intrinsic silicon. *Nano Lett.* **7**, 2051-2055 (2007).
32. Feher, G. & Gere, E. A. Electron Spin Resonance Experiments on Donors in Silicon. I. Electronic Structure of Donors by the Electron Nuclear Double Resonance Technique. *Phys. Rev.* **114**, 1245-1256 (1959).